Investigating the Surface Reactivity of Black Phosphorus

Camille Jackson

A thesis

submitted in partial fulfillment of the

requirements for the degree of

Master of Science in Applied Chemical Science and Technology

University of Washington

2023

Reading Committee:

Alexandra Velian
Bo Zhang
Douglas Reed

Program Authorized to Offer Degree:

Chemistry

University of Washington

Abstract

Investigating the Surface Reactivity of Black Phosphorus

Camille Jackson

Chair of the Supervisory Committee:
Dr. Alexandra Velian
Department of Chemistry

Black phosphorus (bP) a layered 2D allotrope of elemental phosphorus, is a promising material for electronic and catalytic applications, due to its direct, tunable bandgap, high carrier mobility, and relatively reactive basal plane. Although bP was discovered in 1914, knowledge about the surface reactivity remains limited. This work aims to explore different facets of bP reactivity. Chapter 1 provides insight into bP and its unique electronic and chemical properties. Chapter 2 focuses on the use of bP as a building block in van der Waals heterostructures. The electrocatalytic hydrogen evolution reaction (HER) was used to investigate a series of synthesized metal cluster–bP heterostructures. Chapter 3 investigates the possibility of bP as a Lewis base accessing frustrated Lewis pair (FLP) chemistry when paired with a sterically hindered Lewis acid through the activation of small molecules such as H_2 and phenylacetylene (PhCCH).

TABLE OF CONTENTS

LIST OF FIGURES

LIST OF TABLES

ACKNOWLEDGEMENTS

First, thank you to Prof. Alexandra Velian for believing in me and pushing me to challenge myself. Thank you for being kind and supportive as I navigated the ups and downs of this experience. It has meant more to me than I can express. Working in your lab has made me a better scientist and given me skills to move forward and be successful in life. I also want to thank the other members of the Velian group. Your friendship and comradery have made my life brighter. A special thanks to Kendahl, Andrei, and Michael for being my friends, taking me under your wings, and helping me complete this work. And thank you to the University of Washington Chemistry department for giving me this opportunity.

Finally, a big thank you to my family and friends for being my biggest cheerleaders. Thank you, Mom, and Dad, for everything you have done for me. Words cannot express how grateful I am and how much I love you both. Thank you to my siblings for all your support and love. Thank you, Rachel and Allie, for listening to every thought I have ever had, making me laugh, and being the best friends a girl could ask for.

I could not have done this alone. Thank you.

DEDICATION

I would like to dedicate this thesis to my parents, Roger and Rhonda. Thank you for always supporting me in all I do and believing in me 100%. I would not be who I am without you.

Chapter 1. INTRODUCTION TO BLACK PHOSPHORUS

1.1 Overview of Black Phosphorus

Elemental phosphorus exists in three common allotropes: white phosphorus, red phosphorus, and black phosphorus.[1] White phosphorus is made of tetrahedral clusters where each phosphorus atom is covalently bonded to three other phosphorus atoms. It is the most reactive allotrope as it is highly unstable in air and combustible at low temperatures, making it impractical to work with. Red phosphorus is a polymeric allotrope where the tetrahedral clusters found in white phosphorus are linked by a P–P bond between the clusters. While it is more stable and less toxic than white phosphorus, red phosphorus is still highly reactive. It also exhibits low electronic conductivity.

Discovered in 1914 by P.W. Bridgman at Harvard University,[2] black phosphorus (bP) is the most thermodynamically stable phosphorus allotrope despite slow oxidation in air. Its relatively non-toxic nature allows bP to be used in systems like drug delivery.[3] In 1935, Hunltgren and coworkers reported on the crystal structure of bP, revealing it to be an orthorhombic lattice.[4] Later, in 1953, Keyes and coworkers detailed the electronic properties, showing predominantly p-type semiconductivity.[5] After these discoveries, little interest was shown in bP for some time. The discovery of graphene in 2004 caused a rise in interest in van der Waals materials in general, but it wasn't until 2008 that Nilges and coworkers began the "black phosphorus renaissance" with their low-pressure synthesis of high-quality bP crystals.[6]

Black phosphorus is a van der Waals nanomaterial, meaning the sheets are held together by weak van der Waal interactions while individual sheets are made up of covalently bonded, sp^3-hybridized, tricoordinate phosphorus atoms. This bonding causes a corrugated structure where each phosphorus atom has a lone pair exposed on the surface of the sheet as seen in Figure 1.1.

When compared to other 2D materials, the unique corrugated structure of bP has a higher surface area-to-volume ratio. Black phosphorus is used as either a "bulk" material with many layers or a "few-layer" material. The number of layers in the material is controlled through chemical or mechanical exfoliation of the nanosheets. It's corrugated, anisotropic structure separates bP from other van der Waals materials and provides unique electronic, structural, and chemical properties.

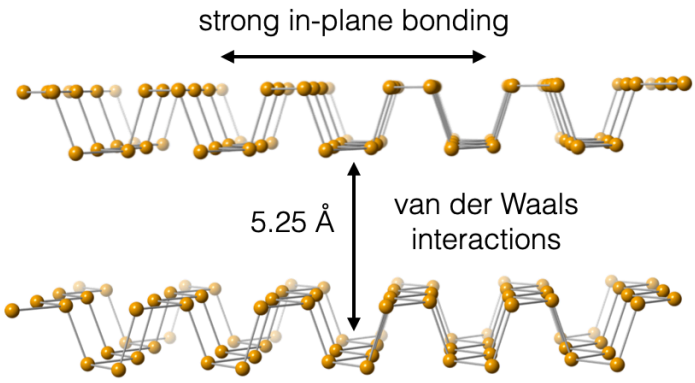

Figure 1.1. Structure of black phosphorus.

Interest in bP is attributed mainly to its electronic properties. Black phosphorus is a semiconductor with a tunable band gap that is dependent on the number of layers in the material, ranging from 0.3 eV in bulk and 2.1 eV in the monolayer. This bandgap range bridges the gap between metallic graphene and other transition metal dichalcogenides (TMDC), making it attractive for mid-IR applicaitons.[7] Black phosphorus is a p-type semiconductor with a high carrier mobility of up to 1000 $cm^2V^{-1}s^{-1}$ compared to other TMDC carrier mobilities.[7] For example, MoS_2 has a carrier mobility of less than 270 $cm^2V^{-1}s^{-1}$.[8] The tunable bandgap and high carrier mobility make bP an ideal material for electronic and optical applications. The chemical functionalization of bP is largely unexplored, and this work aims to fill some gaps in the knowledge in this regard.

1.2 Applications of Black Phosphorus

1.2.1 *Surface Functionalization and Modification*

The available electron lone pairs on the basal plane of bP make it a more receptive surface to modification and functionalization than other 2D materials like graphene. While a good canvas for functionalization, there are challenges that remain due to limitations such as its instability under ambient conditions.[9] There are also challenges to surface modification due to the difficulties in surface characterization and analysis. Methods to covalently modify the bP surface follow methods used for other 2D materials, such as graphene and hexagonal boron nitride (h-BN), but they rely on harsh conditions using iodonium[10] and diazonium salts.[11] Other methods of functionalization, like the Staudinger reaction between bP and 4-benzoic acid, use high temperatures and long reaction times that cause degradation of the nanosheets.[12] This degradation makes characterization difficult as the oxidation of the nanosheets is indiscernible from the functionalized P=N bonds. In 2020, Walz Mitra et al. published a mild protocol for nitrene functionalization that utilizes photolysis to generate a series of nitrenes that can be analyzed using ^{15}N-labelling and DFT in conjunction with other spectroscopic methods to confirm the presence of P=N bond.[13]

To further tune bP's properties, metal nanoparticles (NPs) can be added to the surface. Cho et al. showed that with the addition of Pt NPs, bP was capable of chemically sensing low concentrations of H_2 gas that were not sensed prior to modification.[14] Jeon et al. proposes a hybrid bP/Au NP based photodetector. The addition of Au to bP greatly enhanced the light detection and suppressed dark current due to the difference in work functions.[15] A different study by Qiao et al. also synthesized a hybrid bP/Au NP material-as an electrocatalyst for the oxygen evolution reaction (OER).[16] The addition of metal Au to the semiconducting bP increased the carrier mobility and

catalytic activity. Chapter 2 will explore the addition of metal clusters to the bP surface and its effect on the catalytic activity for the hydrogen evolution reaction.

1.2.2 *bP as a Ligand*

Phosphines are a significant class of ligands used in many catalytic processes due to the tunability of their electronic and steric properties. Black phosphorus appears to behave similarly to molecular phosphine ligands. A study done by Wang et al. showed Pt nanoparticles on bP had strong synergistic ligand effects that greatly increased catalytic activity in HER.[17] Vanni et al. grew Pd NPs on the bP surface and found that bP has a coordination number of 1.7 and is polydentate.[18] The polydentate nature of the bP prevented the aggregation of Pd particles on the surface, leading to an increase in the catalytic hydrogenation of chloronitroarenes. While these studies demonstrate the potential of bP as a ligand, very little work has directly compared the electronic and steric properties of bP.

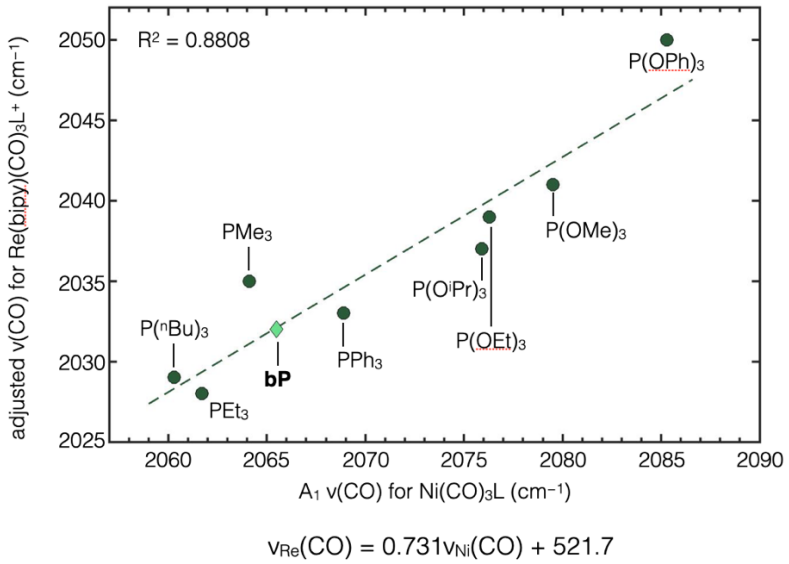

Figure 1.2. Plot of symmetric ν(CO) for $[Re(bipy)(CO)_3Cl(PR_3)][X]$ versus Tolman's Ni complex showing linear correlation ($R^2 = 0.881$).

Previous work in the Velian lab by Dr. Kendahl Walz Mitra further investigates the electronic and steric properties of bP using Tolman's electronic parameter (TEP) and percent buried volume calculations ($\%V_{bur}$) for $Re(bipy)(CO)_3L^+$ compounds as shown in Figure 1.2.[19] The TEP studies suggested that bP has strong σ-donor character with minimal π-accepting character similar to PEt_3. Although the surface of bP is inherently sterically rigid, it is not significantly bulkier than other phosphines. bP can have several binding modes, and these studies focus on the monodentate κ^1 and bidentate κ^2 binding modes. The κ^1 binding mode had $\%V_{bur} = 28\%$, making it not much larger than the 25% for P(*p*-tol)$_3$. The $\%V_{bur} = 43\%$ in the κ^2 binding mode make it comparable to other bidentate phosphines such as bis(diphenylphosphino)propane (dppp) where $\%V_{bur} = 44\%$, or other sterically hindered phosphines like PPh_3 with a $\%V_{bur} = 45\%$.

The lack of steric strain can be attributed to the stepped structure allowing more space for metals along the side of the channel. The electronic and steric properties of bP as a ligand and the lone pairs available on the basal plane make bP a promising material to be used as a catalytic support for single-site catalysts. Chapter 3 will explore the electronic and steric properties of bP acting as a Lewis base.

1.3 EXPERIMENTAL

1.3.1 *Materials*

Unless stated otherwise, all work was performed under an inert atmosphere of N_2 using a Schlenk line or inside of an LC Technology Solutions, Inc. glove box containing <5 ppm H_2O and O_2. All glassware was dried at 160℃ for a minimum of 12 h and cooled under vacuum prior to use. All solvents excluding benzonitrile were purchased from Fischer Scientific. Anhydrous solvents were dispensed from a JC Meyer solvent system and stored over 3 Å molecular sieves (Thermo-Fisher)

for at least 12 h before use. Molecular sieves were previously activated under vacuum at 300℃ for 48 h. Benzonitrile (99%, Alfa Aesar) was degassed for at least 6 hours under vacuum and stored over activated 3Å molecular sieves in the glovebox for a minimum of 72 h prior to use.

Black phosphorus crystals were synthesized using the methods from Nilges.[6] Ultrasonication was performed in a 110W bath sonicator at 40 kHz. Circulation cooling was used to maintain a bath temperature of 22-28℃. Filtrations were performed with EMD Millipore Omnipore hydrophobic membrane filters with a pore size of 0.2 μm.

1.3.2 *Liquid Exfoliation of bP*

Black phosphorus can be exfoliated through liquid exfoliation or mechanical exfoliation to be used for different types of reactions. For liquid exfoliation, the desired amount of bulk bP was weighed into a mortar and pestle and slightly crushed. Any visible particles of red phosphorus and impurities were removed, and smaller impurities were removed in later steps. Using the mortar and pestle again, the bP was crushed into a fine powder that appeared black and slightly silver metallic. The ground bP was added to a round bottom flask. Using a pipette, 1mL of benzonitrile was added to the mortar and pestle and ground thoroughly. Using a separate pipette, the solution was added to the round bottom flask. This process was repeated 3x or until the mortar and pestle was clean. The round bottom flask was then filled with enough benzonitrile to make a 1mg/mL solution.

The flask was sealed and placed in the sonicator. The solution was sonicated overnight to suspend the bP. The sonicator is equipped with a cooling mechanism to prevent the water in the bath from heating and degrading the bP. Once sonication was finished, the solution was centrifuged for 40 min at 300 rpm in Nalgene tubes fit with O-rings to prevent air exposure. The centrifugation causes unexfoliated large particles of bP and unwanted red phosphorus to settle at

the bottom of the tube. The supernatant, a dispersion of small, few-layer bP nanosheets was poured into a vial and stored in the glovebox.

Chapter 2. ELECTROCATALYTIC ANALYSIS OF BLACK PHOSPHORUS HETEROSTRUCTURES

2.1 INTRODUCTION

2.1.1 *bP as a Heterostructure Building Block*

Black phosphorus (bP) belongs to a class of materials called van der Waals materials, along with other layered materials like graphene, MoS_2, and other transition metal dichalcogenides (TMDC), that are at the forefront of research involving electrocatalysis, energy storage, and sensors.[7,20] Black phosphorus has attracted attention due to its high carrier mobility, large surface area, and tunable band gap.[21] With the rising interest in 2D materials, there has also been an increase in research regarding 2D heterostructures.

2D heterostructures advantageously integrate properties from the individual units and create unique physical couplings.[22] 2D heterostructures made of bP and MoS_2 have been shown to be high-performance 2D-semiconductors with unique electron transfer properties.[23] MoS_2 and bP heterostructures have also been shown to be tunable p–n diodes for optoelectrical applications.[24] Several bP containing 2D heterostructures have been applied to catalysis. Mei et al. synthesized bP /nickel hydroxide heterostructure that demonstrated enhanced electron transfer that significantly increased the alkaline oxygen evolution reaction (OER).[25] In-situ grown NiP NPs on bP made by Lin et al. exhibited high electrocatalytic activity and stability for the hydrogen evolution reaction (HER).[26] Black phosphorus has intrinsic electrochemical properties. This was

shown by Wang's electrochemical study of bP where they performed voltammetry on pristine bP.[27] The CV of pristine bP had a significant peak at 0.6 V vs AgCl that corresponds to the irreversible transition from P^0 to P^{5+} with the formation of H_3PO_4.

This work aims utilize electrocatalysis to measure the interactions and catalytic activity of bP heterostructures made using a series of tri-metalated $M_3(py)_3Co_6Se_8L_6$ clusters (tri-M), where M = Cr, Co, Mn, Fe, and Sn, and L= Ph_2PNTol^- (Figure 2.1) as precursors for isolated metal atoms or small metal clusters on bP. The precursor clusters are atomically precise and can be made with a variety of metals, but are not HER active.[28] We would expect to see an increase in catalytic activity with the addition of metal and Co-selenide to the surface, as Co-selenide nanoclusters are known to be HER active.[29–31] Zhang et al. synthesized bP@M heterostructures where M = Co, Pt, and Fe, and measured their catalytic activity using the HER.[32] PtRu nanoclusters on bP were used by Li et al. which was also shown to be effective catalysts in alkaline HER.[33]

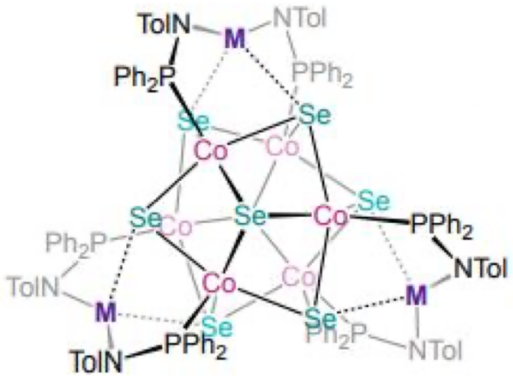

Figure 2.1. Structure of the tri-metalated $M_3(py)_3Co_6Se_8L_6$ (M= Cr, Co, Mn, Fe, and Sn) clusters synthesized by Kephart and Mitchell.[28]

2.1.2 *The Hydrogen Evolution Reaction*

As the need for clean and renewable energy increases, hydrogen gas has gained significant interest as a carbon-free, renewable fuel source. Hydrogen gas is a clean and efficient fuel source that can

be easily produced through water electrolysis which can be performed in a sustainable and large-scale manner.[20] The water splitting process is made up of two processes, or half-reactions: the oxygen evolution reaction (OER), and the hydrogen evolution reaction (HER) as shown in eq 2.1 and eq. 2.2 respectively. Although the HER is a simple reaction, the overpotential is quite high, limiting its ability to satisfy the industrial demand for the reaction.

$$2H_2O \rightarrow O_2 + 4H^+ + 4e^- \quad (2.1)$$

$$4H^+ + 4e^- \rightarrow 2H_2 \quad (2.2)$$

Pt is the most reactive catalyst for the HER and is the most commonly used in the industrial process with an overpotential close to zero.[17] However, the high cost and low abundance of Pt limits its capacity as an industrial catalyst. It is therefore necessary and desirable to find a renewable and low-cost material to serve as a replacement. Electrocatalytic HER has provided a pathway to efficiently develop and analyze potential HER catalysts. The reaction and catalysts can be monitored by basic electrochemical studies.

2.1.3 *Electrochemistry*

Electron transfer is an essential component of inorganic complexes and reactivity. Electrochemistry is a way to probe electron transfer reactions and map the reduction or oxidation of a metal complex. In molecular reactions, when the lowest unoccupied molecular orbital (LUMO) of the oxidant has a lower energy than highest occupied molecular orbital (HOMO) of the reductant, an electron transfer occurs. In electrochemical reactions, the electron is heterogeneously transferred from the electrode to the compound to be reduced when the applied force on the electrode is higher than the LUMO of compound. In both cases the energy difference is the driving force of the reaction.[34]

To investigate when the electron transfer occurs, cyclic voltammetry (CV) is a powerful tool. In a CV, the x-axis is the potential (V), and the y-axis is the measured response in current (*i*). The shape of the CV is referred to as a "duck shape". The shape of the CV depends on several aspects: the applied potential, diffusion rate, and scan rate. In cyclic voltammetry, a forward and backwards sweep of a selected range of potentials is applied. The sweep from high potentials to low potentials tracks the oxidation and is called the anodic trace. The sweep from low to high potentials tracks the reduction and is called the cathodic trace. The direction of the sweep is denoted on the CV with an arrow and is important in reading the CV.

As the potential is applied, the current response is measured at the surface of the electrode. This measurement depends on the concentration of the compound surrounding the electrode, and the diffusion rate of the species in bulk to the electrode surface. The peak in the duck shape occurs when enough potential has been applied to deplete the solution around the electrode of the substrate. This depletion causes the current to drop as more of the substrate diffuses from the bulk solution to the electrode surface. This part of the solution is called the diffusion layer, and it determines the current response. When the direction of the scan is switched, the substrate that had been formed at the surface is then used until it is depleted, causing a similar peak in the reverse scan. If the reaction is not reversible, there will be no peak in the reverse scan. Half-way between these peaks is the point where the concentration of the reduced and oxidized species is the same, and following the Nernst equation, $E = E_{1/2}$.

The last determining factor is the scan rate which controls how fast the potential is applied. As the scan rate is increased, the diffusion layer around the electrode surface is decreased. As discussed above, having a smaller diffusion layer increases the diffusion of unreacted substrate to the electrode, which causes an increase in current response and decrease in peak separation. In

some cases where the reversible reaction is not seen, by increasing the scan rate the reversible reaction becomes visible. In other cases, as the scan rate is decreased, and the peaks separate further, multiple peaks appear and reveal a multi-electron transfer reaction.

When analyzing the activity of a H_2-evolution catalyst by electrochemistry, a common metric of comparison is overpotential (η). Electrochemical HER on any electrode material other than Pt is limited kinetically instead of thermodynamically, and the energy applied to make the reaction occur can be higher than predicted. The extra energy required for the reaction is the overpotential, and it is conceptually similar to activation energy in thermodynamics.[35] HER using Pt catalysts have no overpotential, so it is important that any catalyst being developed for HER must have an overpotential as close to zero as possible.

2.2 Results and Discussion

2.2.1 *Heterostructure Characterization*

To synthesize the bP@Tri-M, the cluster and bP crystals were ground together in a mortar and pestle to form a fine powder. The organic ligands on the clusters were removed by thermogravimetric analysis (TGA), promoting interaction between the bP surface lone pairs and the metal adatoms formed from thermolyzed clusters. Prior to the electrochemical reactions, the bP@Tri-M heterostructures were characterized by TGA, SEM-EDS, and XRD to confirm the formation of the heterostructure. Black phosphorus is prone to oxidation and degradation when exposed to light and air. These characterization methods also confirm that the synthesis was sufficiently mild, remained significantly air-free, and that the bP maintained its crystallinity throughout the synthesis. After characterization, the heterostructures were dispersed in THF by

sonicating the mixture. To make the electrode, the dispersion was drop cast onto carbon paper and annealed.

Thermogravimetric Analysis (TGA)

TGA was completed at 350 °C because the preliminary studies showed that bP degraded above 420 °C, and the clusters showed almost complete loss of organics at 350 °C. During the formation of the heterostructure, we approximated a weight percent loss of 20–30 % due to the loss of organic ligands. As seen in Figure 2.2, the TGA data agrees with that estimate. The ligand removal proceeding as expected is promising data that the addition of the metals on the surface has occurred as theorized.

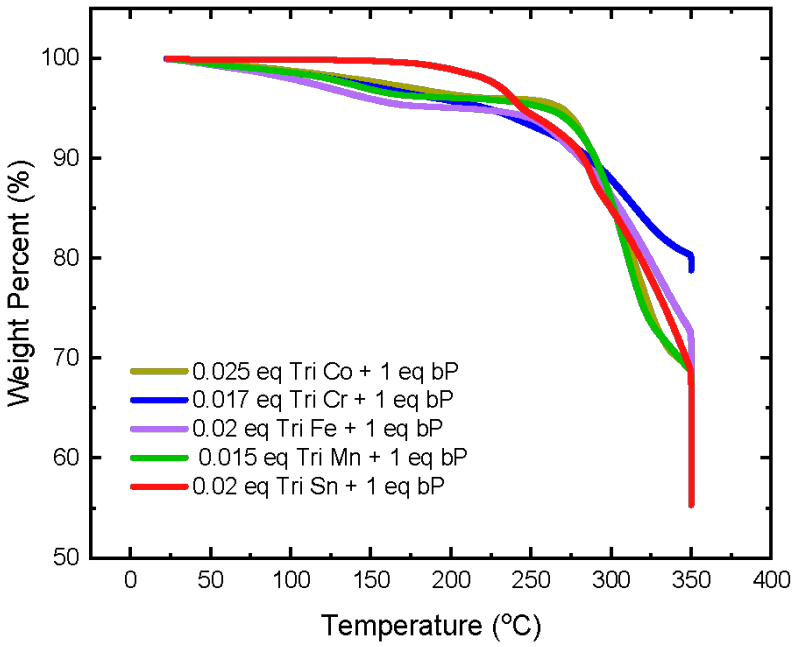

Figure 2.2. TGA of the series of bP@Tri-M formations shows a 20–30 % weight percent loss for all heteromaterials as expected.

Scanning Electron Microscopy–Energy Dispersive Spectroscopy (SEM EDS)

The presence of the metals on the surface of the bP was analyzed using scanning electron microscopy–energy dispersive spectroscopy (SEM EDS). As a layered material, the morphology of bP is laminar. There are non-laminar particles decorating the surface, which EDS mapping

attributes to both oxidation and metal species(Figure 2.3A). The EDS maps of the surface show the presence of Co and Se from the Co_6Se_8 core of the cluster as seen in Figure 2.3B. The distribution of the Co and Se on the bP indicates homogenous coverage of the surface with the metals from the cluster precursor.

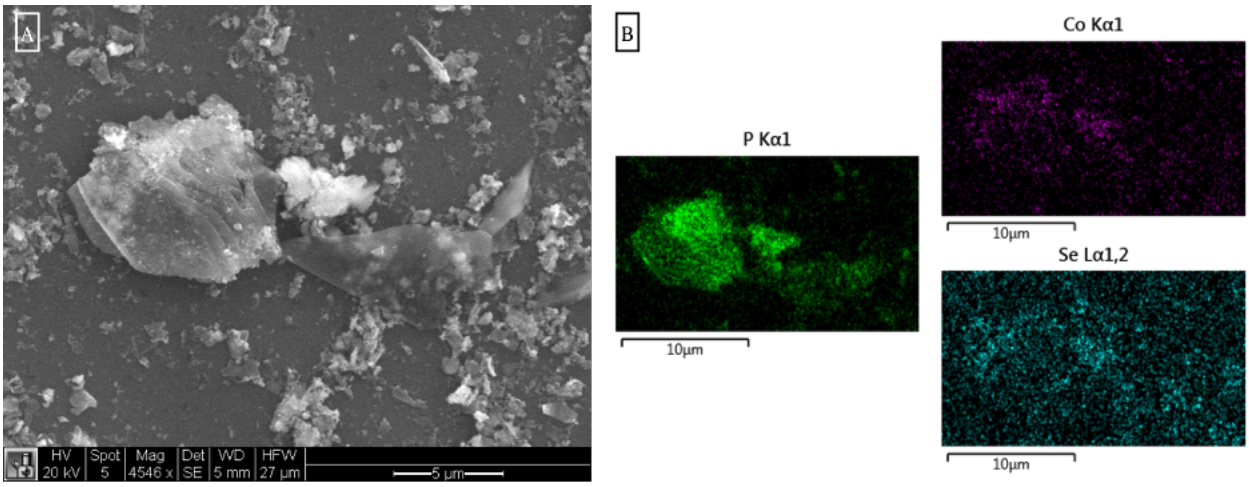

Figure 2.3. A. SEM image of the bP surface decorated with particles. B. EDS mapping of the P, Co, and Se distribution on the bP@Tri-Co surface.

Powder X-Ray Diffraction (XRD)

Powder X-ray diffraction (XRD) was used for phase identification. Post TGA synthesis, the bP@Tri-M clusters show a high intensity (040) bP peak at 34 2θ, which indicates that the bP remains crystalline and does not degrade during synthesis.[6] There is no shift in the peaks from pre to post functionalization, indicating that metals are not intercalating between the bP layers and are predominantly on the surface of the heterostructure. For each functionalized bP heteromaterial, there are new peaks in the 40–60 2θ region that align with metal-selenides and Co-selenides as denoted in Figure 2.4 by (*). Other metal peaks are not seen due to the low concentrations of the metal in the material. There is also peak broadening and peaks from the Kapton tape and Si chip seen in all the XRD data. The peaks were matched using the Inorganic crystal structure database (ICSD).

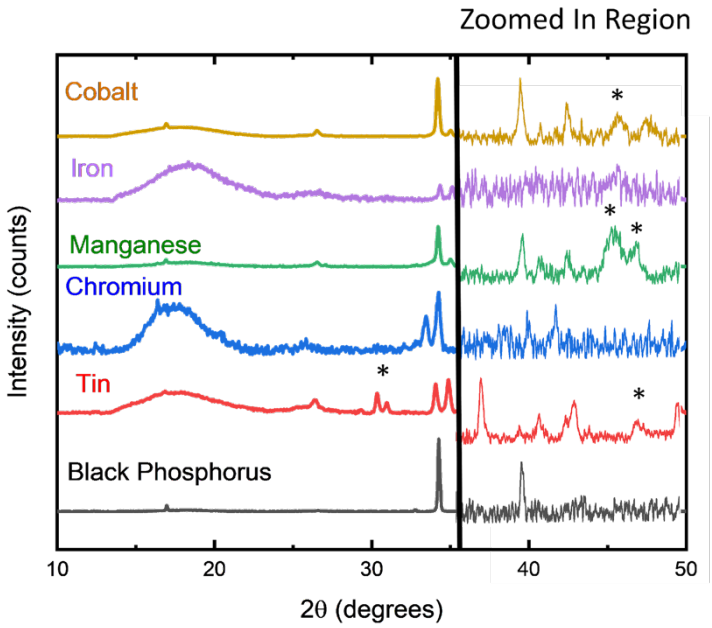

Figure 2.4. Powder XRD spectra of bP@Tri-M heterostructures. The characteristic bP peak at 34 2θ shows no intercalation and that the bP remained crystalline after TGA treatment. Peaks associated with Co-Se species are denoted by (*).

2.2.2 *Electrocatalytic Analysis*

A three-electrode electrochemical H-cell with an electrolyte solution of 0.1 M TBA-PF_6 in dry acetonitrile (MeCN) was used to investigate the electrocatalytic HER activity of the materials. An Ag/AgCl electrode was used as a reference electrode, a Pt wire was used as a counter electrode, and the bP@Tri-M heterostructures on carbon paper were the working electrodes. CVs were taken after subsequent additions of TFA to assay the activity of the bP. Black phosphorus shows more activity than the carbon paper as exhibited in Figure 2.5A. Black phosphorus alone has intrinsic electronic activity that carbon paper does not, so it is expected that it would exhibit better activity. This also showed that the carbon paper as an electrode support would not impact the electrocatalytic studies. Although there is some activity prior to the addition of the metal clusters, the overpotentials are extremely high. To determine the optimal amount of bP, electrodes were

made with varying loadings of 0.25, 0.50, and 1.00 mg/cm^2. Figure 2.5B clearly shows that at all acid concentrations, the electrode with 0.50 mg/cm^2 loading of bP had the lowest overpotential, so all other electrodes were synthesized to have this optimal loading.

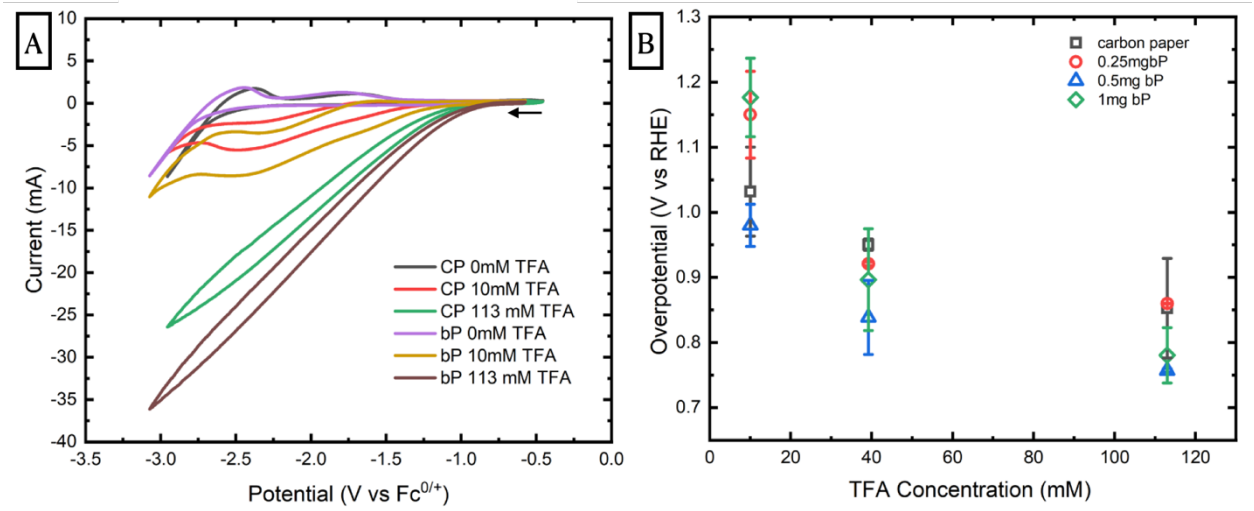

Figure 2.5. A. CVs of carbon paper and bP on carbon paper electrodes at different concentrations of TFA shows an increase in activity as acid concentration increases. All scans were taken with a scan rate = 100 mVs^{-1}, a scan window of 0.0 V to -3.0 V and were absolutely referenced to ferrocene. B. Overpotential comparison of carbon paper and various concentrations of bP on carbon paper at different TFA concentrations.

The overpotential was calculated following methods developed by Fourmond et al., who outlined a standardized process of determining overpotentials for HER.[35] Their methods are for homogeneous HER catalysts, but have been adapted for our purposes. The cathodic sweep was fit to a sigmoid curve, and the first derivative was taken. The peaks in the derivative indicate an electron transfer reaction, in this case the reduction of H^+ to H_2, occurred. The potential at these points was referenced to ferrocene and 15mV was subtracted according to studies by Treimer and Evans.[36] One difficulty to note when using overpotentials as a metric of comparison is the effect of homoconjugation. In weak acid, like acetonitrile, there reaches a point where the acid concentration is high enough that the acid (AH) and its conjugate base (A^-) begin form a stable adduct, as seen in eq. 2.3.

$$2AH + A^- \rightarrow AHA^- + \frac{1}{2}H_2 \quad (2.3)$$

$$AHA^- + e^- \rightarrow 2A^- + \frac{1}{2}H_2 \quad (2.4)$$

This AHA^- adduct also undergoes an electron transfer reaction (eq. 2.4) that can be seen in the first derivative of the reduction wave as the addition of a second reduction peak at a -more cathodic potential than the HER electron transfer. In some cases, the separation of the peaks becomes less defined, forming a singular peak that is between the two values.

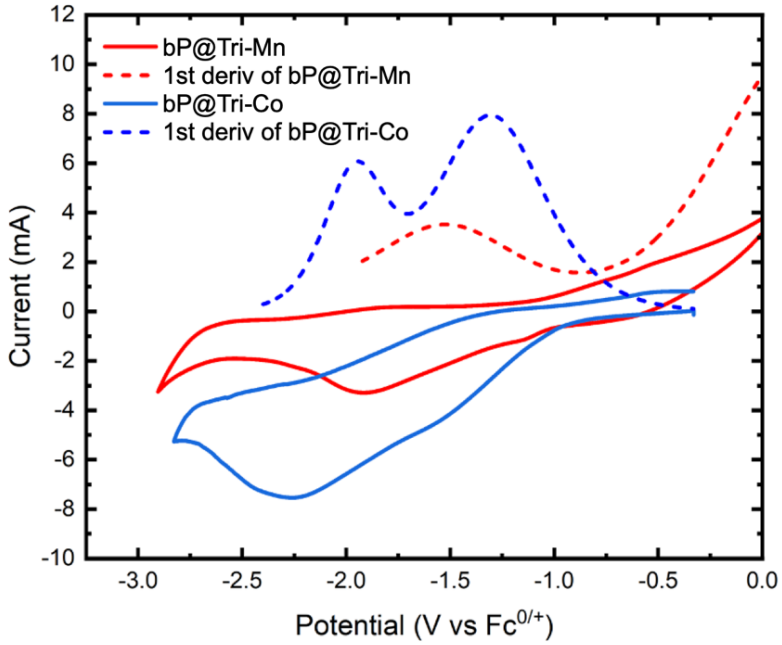

Figure 2.6. CVs and first derivative of bP@Tri-Mn and bP@Tri-Co electrodes with a TFA concentration of 10 mM. CVs were taken with a scan rate = 100 mVs^{-1}, a scan window of 0.0 V to -3.0 V and referenced to ferrocene.

This is clearly demonstrated in the first derivatives shown in Figure 2.6 where there are two clear peaks in the bP@Tri-Co first derivative, but only one peak in the bP@Tri-Mn first derivative that is slightly shifted. This is important to note because it gives the appearance of an overpotential that is higher than the actual value. For this study there were several clusters where this merging of peaks was observed, but overall, it was found to be insignificant in the scope of the study. Although the values are skewed, the general trends remain the same, so homoconjugation was not considered

in the calculation of the overpotential. For future studies, decreasing the scan rate could help separate the peaks. Fourmond also provides more complicated calculations on how to navigate working with a system with high amounts of homoconjugation as well as more complicated equations to process the data.

Assaying the activity of an H_2-evolving catalyst using cyclic voltammetry at the surface of an electrode is done by increasing the concentration of a weak acid being used as a proton source, in this case acetonitrile. As the acid concentration increases, the appearance of an irreversible catalytic wave that corresponds to the reduction of protons to H_2, is a measurable change in the electrochemical response of the catalyst. Figure 2.7 illustrates this point well, as the reduction wave significantly increases with the increase of the TFA concentration. This effect is seen in the CVs for all the electrodes, so only one representative graph is provided here. The overpotential was calculated for each heterostructure at each acid concentration. The overpotential values are shown in Table 2.1.

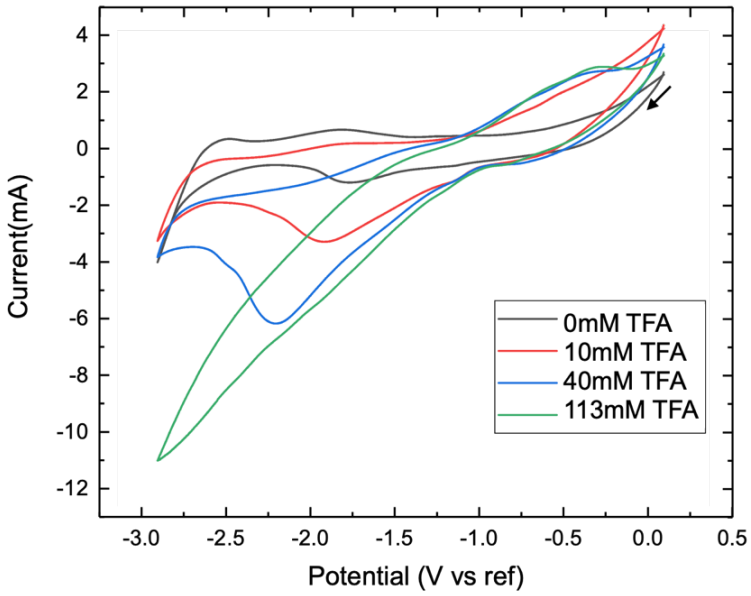

Figure 2.7. CV of bP@Tri-Mn at 0, 10, 40, and 113 mM of TFA showing an increase in current as TFA concentration increases. All CVs were taken with a scan rate = 100 mVs^{-1}, a scan window of 0.0 V to -3.0 V and were absolutely referenced to ferrocene.

Table 2.1 Overpotential (mV) values for each heteromaterial at 10, 40, and 113 mM of TFA.

	Overpotential (mV)		
Material	10 mM TFA	40 mM TFA	113 mM TFA
bP@Tri-Co	864	669.145	627.65
bP@Tri-Fe	2176.58	2346.000	2330.750
bP@Tri-Cr	988.917	1154.167	1383.750
bP@Tri-Mn	799.167	1175.250	1501.167
bP@Tri-Sn	2391.250	2211.250	2282.500
bP@Tri-CP	975.167	881.833	1107.333

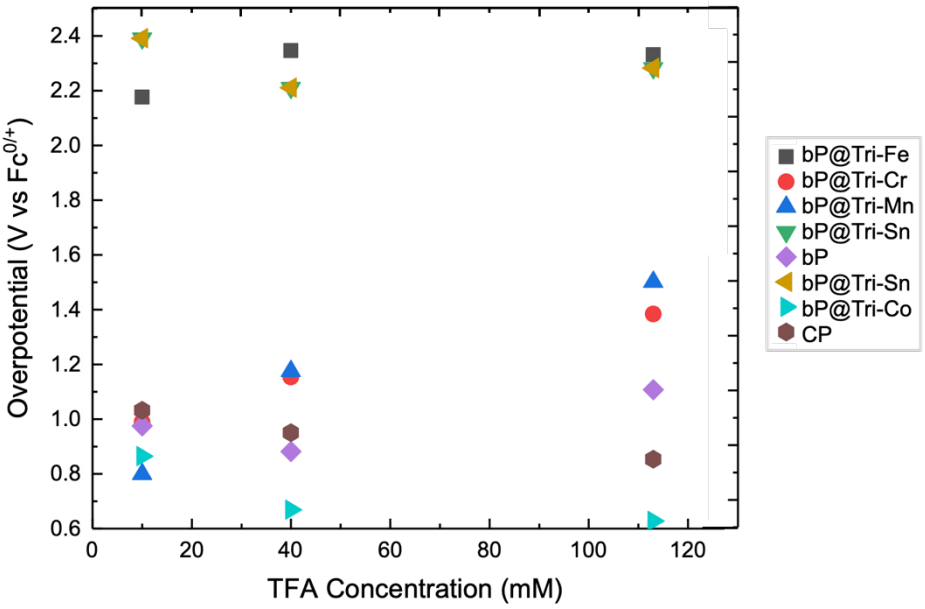

Figure 2.8. Overpotential (V vs $Fc^{0/+}$) comparison for all the synthesized heterostructures at 10 mM, 40 mM, and 113 mM of TFA.

Figure 2.8 shows a comprehensive comparison of the overpotentials of all the heterostructures at each of the three acid additions. Overall, bP@Tri-Co exhibited the lowest overpotentials. The dominate species seen in the XRD and SEM-EDS for each material were Co-selenides. If these Co-selenides are the active species, the tri-Co cluster would contribute more to the active species

than the other metals, effectively increasing the catalytic activity the most. The XRD showed the appearance of metal-selenides in the other clusters, which could be impacting the formation of the active Co-selenides in the other heterostructures. There is also precedence in the literature for HER active Co-selenides, making it a reasonable conclusion that this would be the active species.[29–31]

While bP@Tri-Co performed the best, the overpotentials for all the heterostructures are far too high to be effective HER catalysts, with some performing worse than pristine bP. Despite the poor performance of the catalysts, the electrochemical study was effective at screening the catalytic activity.

2.3 CONCLUSIONS

The tri-metal cluster on bP heterostructure was successfully synthesized. TGA confirmed the expected loss of organic ligands needed for form the heterostructure. SEM-EDS showed the appearance of particles on the otherwise laminar surface of bP after TGA synthesis. The elemental analysis from SEM-EDS showed homogeneous coverage of Co and Se on the bP surface. XRD confirmed that the heterostructure is crystalline, and the bP remained crystalline and did not degrade during synthesis.

Overall, the bP@Tri-Co had the lowest overpotential with a value of 627.5mV. This could be attributed to the extra Co atoms contributing to the active Co-Se species. The addition of the tri-Co clusters successfully lowered the overpotential for the reaction and increased the HER activity of bP. However, these overpotentials are still too high to be effective industrial catalysts. While the overpotential was not lowered significantly, there was a measurable difference between the various bP@Tri-M materials, showing that electrochemistry is an effective way to screen potential catalyst activity.

2.4 EXPERIMENTAL

2.4.1 *Materials*

Unless stated otherwise, all work was performed under an inert atmosphere of N_2 using a Schlenk line or inside of an LC Technology Solutions, Inc. glove box containing <5 ppm H_2O and O_2. All glassware was dried at 160℃ for a minimum of 12 h and cooled under vacuum prior to use. All solvents excluding benzonitrile were purchased from Fischer Scientific. Anhydrous solvents were dispensed from a JC Meyer solvent system and stored over 3 Å molecular sieves (Thermo-Fisher) for at least 12 h before use. Molecular sieves were previously activated under vacuum at 300℃ for 48 h. Benzonitrile (99%, Alfa Aesar) was degassed for at least 6 hours under vacuum and stored over activated 3Å molecular sieves in the glovebox for a minimum of 72 h prior to use.

Black phosphorus crystals were synthesized using the methods by Nilges.[6] Ultrasonication was performed in a 110 W bath sonicator at 40 kHz. Circulation cooling was used to maintain a bath temperature of 22-28℃. Filtrations were performed with EMD Millipore Omnipore hydrophobic membrane filters with a pore size of 0.2 μm. Tetrabutylammonium hexafluorophosphate (≥99.0%, Sigma), trifluoroacetic acid (99%, Sigma), and ferrocene (Sigma) were used for electrochemical analysis.

2.4.2 *Instrumentation*

Scanning electron microscope images were obtained on a FEI Sirion XL30 Scanning Electron Microscope (SEM) integrated with an Oxford Instruments Energy Dispersive X-ray Spectrometer (EDS). Powder X-ray diffraction (PXRD) spectra were acquired on a Bruker D8 Discover Powder X-ray diffractometer with a large-area Pilatus 100K large-area 2D detector under ambient conditions. Kapton tape was used to cover wafers for XRD. For analysis (Powder-XRD and

SEM/EDS), test-grade Si wafers (University Wafer) were cut, rigorously washed by sequential ultrasonication with detergent (Si only), water (Si only), acetone, and isopropanol, and then oven-dried overnight at 150 °C prior to use. Suspensions of various bP products in tetrahydrofuran (THF) were drop-cast onto clean silicon wafers and annealed for 2–5 min at 80 °C before analysis for SEM/EDS or were directly deposited as dried powders for XRD. Thermal Gravimetric Analysis was performed using a TGA Q5000 from TA instruments under nitrogen flow.

2.4.3 *Synthesizing The Heterostructure*

A van der Waal's heterostructure requires two 2D crystalline materials to be stacked on top of each other. For our purposes, the two crystals being used were bP and a tri-metalated nanocrystal with a Co_6Se_8 core. A tri-Co, tri-Cr, tri-Sn, and tri-Fe cluster were each used in the synthesis. The bP nanosheets were made in the Velian lab by Michael Riehs. The tri-metalated nanocrystals were made and characterized by various members of the cluster team in Alexandra Velian's lab at the University of Washington following their synthesis protocols and were provided for these experiments.[28] The cluster powders were sealed in scintillation vials and taped to ensure an air-tight seal during transportation.

To form the heterostructure, the pristine bP crystals and the nanocluster crystals were added to a mortar and pestle and ground until a well combined, grayish fine powder. At this point the powder no longer contains any of the shine and luster that is seen in crushed pristine bP. Once well combined, the mixture was weighed and placed in vials that were sealed and taped to ensure an air-free environment during transfer to the TGA instrument. The powder was briefly exposed to air during transfer into the TGA, but it is assumed that it is not sufficient exposure to cause any degradation of the sample based on ambient stability studies done by van Druenen.[9] TGA decomposition was then performed on the powder. The temperature program ran from room

temperature to 350 °C at a rate of 10 °Cmin^{-1} and then had an isothermal hold at 350 °C for 10 min.

Decomposition during the TGA program burns off the ligands on the cluster and causes the metals to bind with the lone pairs on the surface of the bP. After the decomposition, the bP/cluster heterostructure was added to THF to have a concentration of 1mg/mL and sonicated for several minutes to disperse the powder in the THF. This solution was then used to prepare the electrodes.

2.4.4 *Electrode Synthesis*

All syntheses and reactions took place in an air-free environment in an N_2 filled glovebox. The support for the electrode was carbon paper. The carbon paper was prepped for electrode synthesis by soaking in H_2SO_4, followed by soaking in water, acetone, then IPA. After sufficient soaking, the carbon paper was dried in the oven to remove any solvent. To synthesize the electrode, the carbon paper was cut into squares approximately 1cm x 1cm. Four pieces of the carbon paper that were roughly the same size were placed in a glass petri dish. In the glass dish, the electrodes were numbered and labeled. The glass petri dish was then placed on a hot plate on low heat. Using a pipette, 10 drops of the previously synthesized bP/M-cluster solution was drop-casted onto each of the carbon paper electrodes to give a loading of about 0.5 mg/cm^2. The drop-casting was done slowly, adding 2-3 drops at a time, and waiting until the solvent evaporated slightly before the adding the next set of drops. This process prevents the bp/cluster solution from flooding the carbon paper and leaking into the petri dish. Once all 10 drops were added, the electrodes were annealed to remove any excess solvent and ensure that the bp/cluster was adsorbed to the surface of the carbon paper. After annealing, the electrodes were removed from the heat and cooled to room temperature before use.

2.4.5 *Hydrogen Evolution Reaction*

All the hydrogen evolution reactions were done in a glass electrochemical H-cell that is cleaned and dried thoroughly between each reaction. Inside the glove box, both sides of the H-cell were filled with 25 mL of an electrolyte solution of 0.1 M TBA-PF_6 in dry MeCN. Unlike other HER experiments, this reaction takes place in an organic solvent opposed to an aqueous solvent, so a hydrogen source must be added. The proton source for this reaction was a solution of 100 mM trifluoroacetic acetic acid (TFA) in MeCN. The reaction setup used a three-electrode system. On the right side of the H-cell was a platinum wire used as the counter electrode (CE). Separated from the right side by a glass frit, on the left side was an Ag/AgCl reference electrode (RE), the functionalized carbon paper electrode as the working electrode (WE), and a stir bar. The three electrodes were placed in the H-cell, so they were not touching each other or the glass walls. All three electrodes were connected to an external computer and a Gamry potentiostat outside the glovebox via a custom wire setup that ran through the side of glove box.

Before starting the measurements, the open circuit potential (OCP) was measured until stable. This OCP value was then used to precondition the CVs. All CVs were performed under static conditions with a scan rate of 100 mV/s and step size of 0.5 V. Four scans were taken, each from -3.0 V to 0 V back to -3.0 V. The solution was stirred for 30 s before inserting the WE to ensure homogeneity. After the 4 scans were completed, the WE was removed for the addition of the TFA solution. The 100 mM TFA solution was added by syringe in three separate amounts, 0.5 mL, 1 mL, and 3 mL, to test the electrodes at various concentrations of TFA. After the addition of the TFA, the solution was stirred for 30 s before reinserting the WE for the next measurement. For each acid addition, the four electrodes were scanned four times. When changing electrodes, care was taken to only handle the edge of the carbon paper with the Teflon tipped forceps to avoid

damage to the electrode surface. After the final acid addition, a small amount of ferrocene was added. Each electrode was scanned a final four times All values were referenced to the final ferrocene value.

2.4.6 *Working up the data*

All data was worked up following the equations outlined by Fourmond et al.[35] All data analysis was done using the data analysis software Origin. All four runs for each electrode per acid addition were individually processed. Because the formation of H_2 gas is a non-reversible process, we are only interested the reduction half reaction. The forward scan was fitted with a sigmoid function. The sigmoid fit in origin is called BiDoseResp, and the line is fit until it is converged with an R^2=0.99. The first derivative is taken of the fit line using the Origin derivative function. Using the peak fit function, any peaks in the derivative are fit to a gaussian function until converged to an R^2=0.99 to find the exact peak center. This same line and peak fitting process was repeated for the ferrocene additions for each of the electrodes.

The value of the peak centers was used to calculate the overpotential. First, 15 mV is subtracted from the acid addition peak centers because Treimer and Evans found that the inflection point used for overpotential in stationary cyclic voltammograms is systematically 15 mVs high.[36] Finally, the calculated value was referenced to the ferrocene peak center value and the absolute value was taken. The four values per electrode for each acid addition were averaged to give one value for each electrode per acid addition. The standard deviation of each overpotential was also calculated.

Chapter 3. BP BASED FRUSTRATED LEWIS PAIRS

3.1 INTRODUCTION

Lewis acid/base interactions are a key principle of chemistry. Lewis pair chemistry is based on a donor-acceptor interaction where an electron rich Lewis base donates electrons to an electron deficient Lewis acid, forming a bond. Phosphines are common Lewis bases due to the lone pair.[37] As mentioned in section 1.2.2, black phosphorus (bP) is a good σ-donor, suggesting it can act as a decent Lewis base. Tofan et al. showed that the surface of bP can be modified with group 13 Lewis acids including BBr_3, $AlCl_3$, and $GaCl_3$.[38]

In 2007, Stephan and coworkers discovered a new way to consider Lewis acid/base interactions.[39] In their studies, they showed that by adding large, sterically hindering ligands to both the Lewis acid and base, they can prevent the formation of a typical bond. This leads to unquenched Lewis acidity and basicity that is able to accept and donate additional electrons from other small molecules.[40] To describe these new Lewis acid/base interactions, they coined the term "frustrated Lewis pairs" (FLPs).

It was found that phosphines such as Mes_3P and tBu_3P are sufficiently bulky Lewis bases to be paired with boranes like p-$(Mes_2PH)C_6F_4(BH(C_6F_5)_2)$ or $B(C_6F_5)_3$ (BCF) to form the FLP. In subsequent studies, McCahill et al. and Dureen et al. showed that frustrated pairs are capable of activating H_2, olefins, alkynes, and other small molecules.[39,41,42] The FLP, through the activation of H_2, was shown to successfully hydrogenate a range of substrates including imines, aziridines, enamines, silyl enol ethers, and aromatics.[43] These reactions are done under homogeneous conditions, but a heterogeneous FLP would allow for better catalytic recovery, and easier product purification. There is precedent for FLPs on layered surfaces such as AlOOH, and

$In_2O_{3-x}(OH)_y$.[44,45] These examples rely on defect or vacancy engineering in the materials to bind the Lewis acid. Black phosphorus, on the other hand, would act more as a molecular approach by relying on steric hindrance to form the FLP, and provide a metal-free, heterogeneous alternative for FLP chemistry.

The percent buried volume ($\%V_{bur}$) of Mes_3P and tBu$_3$P are reported as 26.7% and 47.6% respectively.[46] As mentioned in section 1.2.2, the $\%V_{bur}$ for bP was calculated to be 28% in the κ^1 binding mode. Although significantly less bulky than tBu$_3$P, bP has a similar bulkiness to Mes_3P. Because the FLP interaction is dependent on bulkiness, it reasons that because Mes_3P is sufficiently bulky, bP would also be able to act as the Lewis base in a FLP. This work aimed to discover if bP could act as a FLP with BCF and activate small molecules including H_2 and phenylacetylene (PhCCH).

The activation of alkynes is an important reaction pathway for many synthetic organic reactions.[47] The use of transition metal catalysts with terminal alkynes is known to facilitate C–C coupling for reactions like the alkynylation of aldehydes.[48] Transition metals are also shown to facilitate hydrosilylation, hydroboration,[49] and hydrophosphination[50] of alkynes, but little has been done with main group species. Dureen and Stephan showed the activation of terminal alkynes through FLPs in a metal free reaction.[41]

3.2 Results and Discussion

In their study on terminal alkyne activation, Dureen and Douglas saw a mixture of different products depending on the steric hindrance of the phosphine that provided new insight to the chemical capabilities of FLPs and classical Lewis pairs.[41] A FLP was observed by combining tris-pentafluorophenyl boron ($B(C_6F_5)$ or BCF) and their most sterically hindered phosphines, tri-tert-

butylphosphine (*t*But$_3$P) and tri(*o*-tolyl)phosphine (*o*-tol$_3$P). The *t*But$_3$P FLP formed an alkynylborate salt made up of an alkyne–BCF adduct and protonated phosphine. The *o*-tol$_3$P FLP formed a zwitterionic product formed by the addition of the FLP across the triple bond with the phosphine adding to the substituted end and the borane adding to the C–H end of the terminal alkyne in an *E* configuration. Interestingly, the less sterically hindering tri-phenylphosphine (Ph$_3$P) also formed the zwitterionic species despite forming a classical Lewis acid/base adduct instead of a FLP. This study suggests that classical Lewis pair and FLP reactivity are not mutually exclusive, and a range of FLP reactivity can be achieved through classical avenues that were previously disregarded.

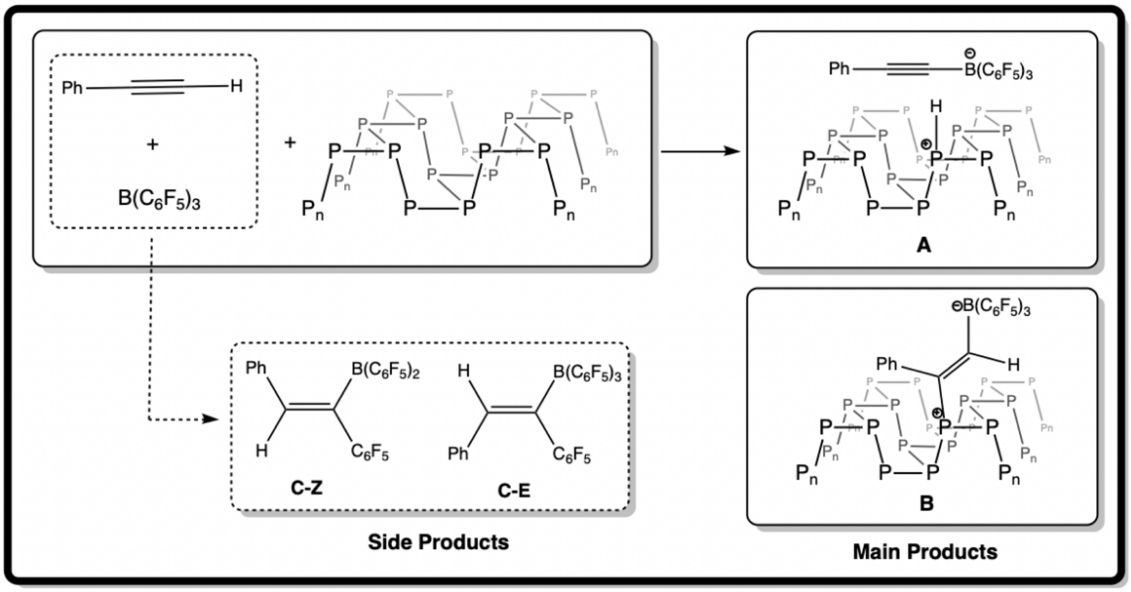

Figure 3.1. Proposed FLP reaction for the activation of PhCCH by bP + BCF gives products **A** and **B**. A competing side reaction of PhCCH and BCF forms stereoisomers **C-Z** and **C-E** as side products.

Black phosphorus is Lewis basic and forms classical adducts with group 13 Lewis acids, but it is not as sterically hindered as *t*But$_3$P or *o*-tol$_3$P.[38] The work by Dureen and Douglas begs the question of if bP, which typically acts as classical Lewis pair, can access the FLP reactivity if combined with a bulky enough borane. Figure 3.1 details the products that would be expected

depending on the Lewis reactivity. If bP–BCF is able to access FLP reactivity, the predicted products are **A** and **B**. To test the nature of the reactivity, reactions were setup using bP as the Lewis base, BCF as the Lewis acid, and PhCCH as the terminal alkyne.

It is important to note that BCF and PhCCH are known to react to form stereoisomers **C-Z** and **C-E** in a competing reaction.[51] This presence of this competing reaction was tested by running a reaction under the same conditions but excluding bP. Upon combination of PhCCH and BCF, the solution immediately turned a deep red color indicating the formation of **C-Z** and **C-E**. As the reaction was left to stir, the color faded to yellow. The red reaction mixture was analyzed by ^{19}F-NMR and compared to ^{19}F-NMR values for the expected products by Jiang et al.[51] The peaks corresponded well with the values provided by Jiang, confirming the formation of **C-Z** and **C-E**. The peak assignments are listed in Table 3.2. Assignment of ^{19}F-NMR peaks for PhCCH+BCF control reaction based on peak assignments by Jiang et al.[51]

Table 3.2. Assignment of ^{19}F-NMR peaks for PhCCH+BCF control reaction based on peak assignments by Jiang et al.[51]

Shift (ppm)	Assignment	Compound
128.55	*o*-C_6F_5 of $B(C_6F_5)_2$	**C-E**
129.78	*o*-C_6F_5 of $B(C_6F_5)_2$	**C-Z**
138.6	*o*-C_6F_5 of C_6F_5	**C-Z**
142.21	*o*-C_6F_5 of C_6F_5	**C-E**
145.03	*p*-C_6F_5 of $B(C_6F_5)_2$	**C-E**
146.13	*p*-C_6F_5 of $B(C_6F_5)_2$	**C-Z**
152.76	*p*-C_6F_5 of C_6F_5	**C-E**
154.18	*p*-C_6F_5 of C_6F_5	**C-Z**
160.17	*m*-C_6F_5 of C_6F_5	**C-Z**, **C-E**
161.28	*m*-C_6F_5 of $B(C_6F_5)_2$	**C-Z**, **C-E**

3.2.1 *bP–BCF Lewis Adduct*

Before testing the reactivity of bP and BCF, we needed confirmation that they form a Lewis adduct. To form the adduct, 1 eq of bP and 1.25 eq of BCF were combined in toluene and sonicated for 2 days. After filtering and rinsing thoroughly, excess solvent was removed by vacuum, and the resulting powder was analyzed. We have found that an effective way to characterize the functionalization of bP is diffuse reflectance infrared Fourier transform spectroscopy (DRIFTS) using the KBr pellet method. The DRIFTS spectrum exhibits good overlap of peaks in the 1000–1700 cm^{-1} region (Figure 3.2). These peaks are attributed to F–C bonds in BCF and are not seen in pristine bP, indicating that a bP–BCF adduct was successfully synthesized.[52]

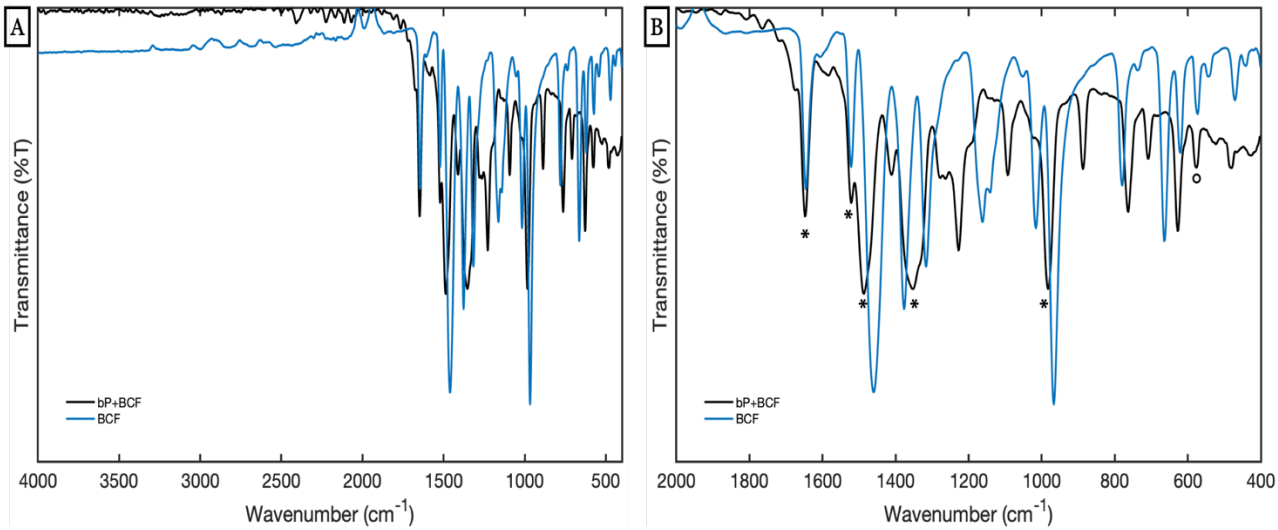

Figure 3.2. A. Full DRIFTS spectrum of bP–BCF Lewis adduct overlayed with BCF starting material. B. Zoomed in 400–2000 cm^{-1} range with C–F stretches denoted by (*) stretches, and P–B stretches are denoted by (o). The presence of C–F stretches on the bP indicate the formation of a bP–BCF adduct.

While the DRIFTS experiment indicates an interaction between bP and BCF, the nature of the interaction remains unclear. Welch et al. showed the evidence that phosphines can perform *para*-nucleophilic aromatic substitution on BCF, forming a zwitterionic phosphonium borate where one of the *para*-fluorine on one of the pentafluorophenyl groups is substituted with the phosphine.[53] If

the *para*-aromatic substitution reaction were occurring, there would be a P=C stretch in the range of 1180–1230 cm^{-1}, which we do not see.[54] The peak at 560 cm^{-1}has overlap with BCF peaks but is also where P–B stretches are seen. This data suggests that a traditional Lewis pair was formed between bP and BCF.

3.2.2 *Activation of Phenylacetylene*

The phenylacetylene reactions took place in the glove box under air-free conditions. The three components were combined in toluene and stirred. The reaction changes color to red immediately but fades to yellow over time as the reaction proceeds. The color change to red corresponds with the formation of the **C-Z** and **C-E** isomers as mentioned earlier.

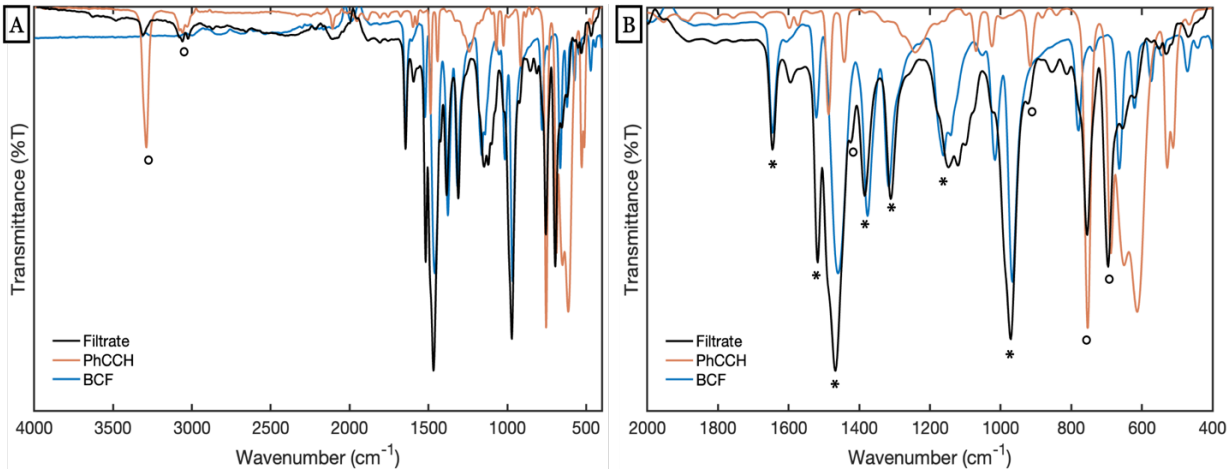

Figure 3.3. A. Full DRIFTS spectrum of reaction filtrate after the reaction of bP with BCF and PhCCH overlayed with BCF and PhCCH starting materials. B. Zoomed in view of 400–2000 cm^{-1} showing peaks corresponding to starting material. The BCF C–F stretches are denoted by (*), and the PhCCH stretches are denoted by (o).

An aliquot of the reaction mixture was filtered into a vial and analyzed using attenuated total reflectance (ATR). We know the formation of the **C-Z** and **C-E** isomers occurred from the initial color change, so the IR spectra should reveal if the isomers or unreacted starting materials remained in solution. Figure 3.3 shows a comparison of the reaction filtrate to BCF and PhCCH

starting materials. The prominent peak at 3290 cm^{-1}, which corresponds to the terminal C–H bond on the alkyne, has greatly diminished but has not disappeared. The peaks in the 1000–1600 cm^{-1} range match very well with the C–F stretches from BCF. If **C-Z** and **C-E** were present in solution the small peak at 3060 cm^{-1}, which is the alkene C–H stretch, would presumably be large. However, the peak is small, so it appears to be from the PhCCH. Because the color of the solution changed from red to yellow and starting material is present in the mixture, perhaps the formation of **C-Z** and **C-E** is a reversible process. The diminishing of the terminal C–H bond is a promising indication that the activation reaction is occurring to some degree.

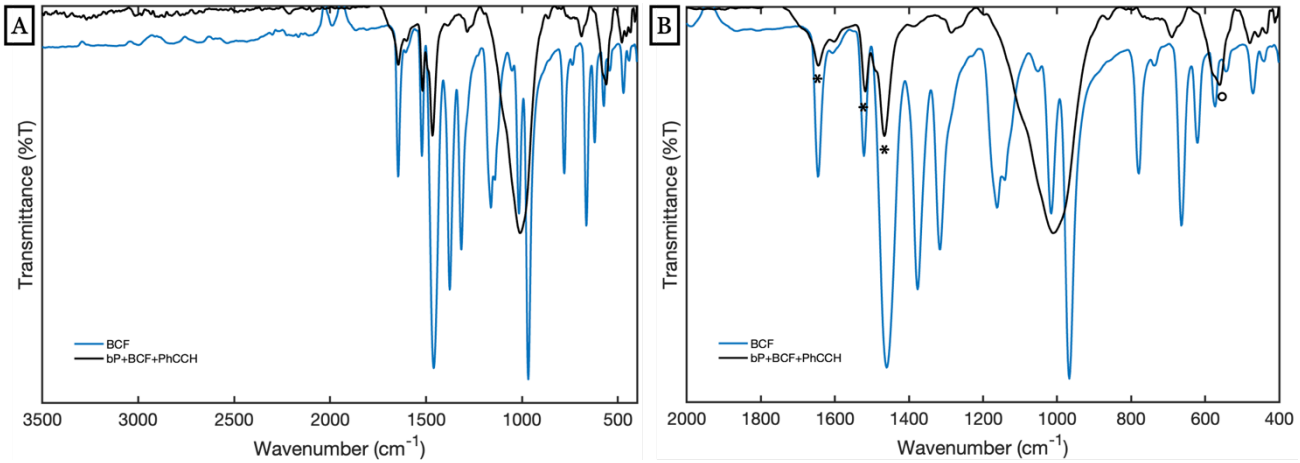

Figure 3.4. A. Full DRIFTS spectrum of bP–BCF Lewis adduct post reaction with PhCCH overlayed with the BCF starting material. B. The 400–2000 cm^{-1} region of the spectrum shows the corresponding BCF peaks with C–F bonds denoted by (*) and the P–B bond denoted by (o).

The post-reaction bP was analyzed using DRIFTS (Figure 3.4). Post-reaction, the bP spectrum only has a few peaks. If product **A** had been formed through a FLP pathway, we would expect to see a C≡C stretch around 2100 cm^{-1} and a P–H stretch around the 2200–2400 cm^{-1}range. The lack of peaks in the 2100–2400 cm^{-1} region indicates that **A** was not formed. There are no peaks in the C–H stretch in the 3100 cm^{-1} range that would indicate the formation of **B**, however, this is not conclusive evidence. The bP DRIFTS spectra have a large peak that dominates the 3000

cm^{-1} range but is removed through a series of background corrections. It is possible that some small peaks would get lost in this process.

Although we cannot confirm that **B** was not formed, the peaks that are present point towards the formation of a bP–BCF adduct being the post-reaction material. The large peak at 1012 cm^{-1} looks like it could be attributed to some the C–F bonds in BCF, but this peak is commonly seen in bP samples and is from oxidation of bP. However, the peaks at 1468, 1517, and 1646 cm^{-1} correspond very well with the red shifted C–F BCF bonds. The peak 565 cm^{-1} is in the region that a P–B stretch would appear. If the *para*-aromatic substitution reaction were occurring, there would be a P=C stretch in the range of 1180–1230 cm^{-1}, which we do not see.[54] The absence of this peak and the presence of a P–B stretch suggests that the substitution reaction does not occur, and a traditional Lewis pair adduct is formed. Based on the data, it also appears that as a classical Lewis pair, bP and BCF are not able to activate terminal alkynes like phenylacetylene.

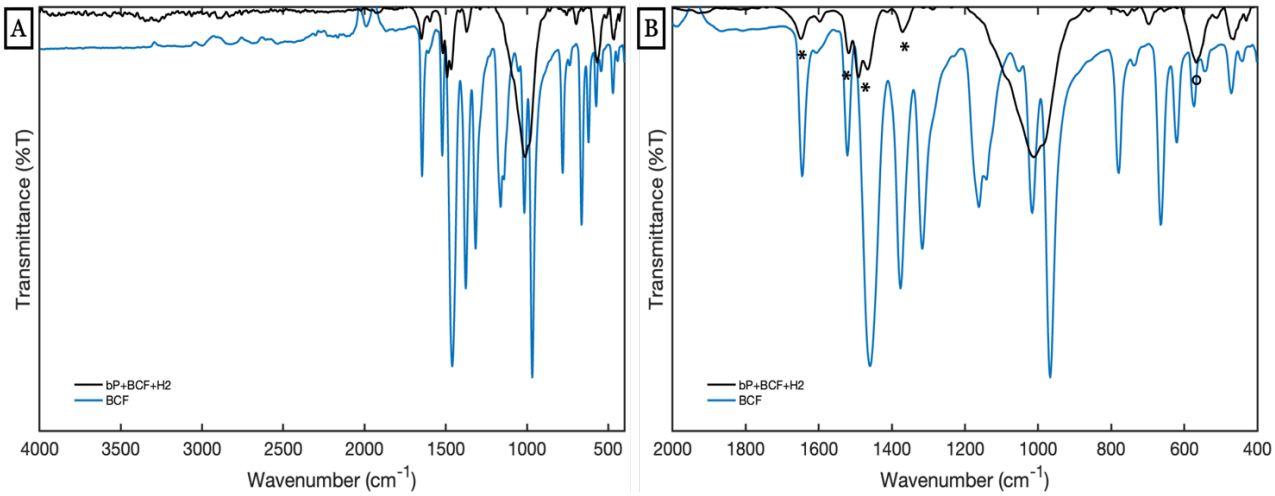

Figure 3.5. A. Full DRIFTS spectra of bP–BCF Lewis adduct post reaction with H_2 overlayed with BCF starting material. B. Zoomed in 400–2000 cm^{-1} region of the spectrum. The C–F bonds from BCF are denoted by (*), and the adduct's P–B bond is denoted by (o). No B–H or P–H stretches are seen in the 2200–2400 cm^{-1} range, confirming that H_2 was not activated.

Other small molecule activation reactions were run using H_2. The bP and BCF solution was sparged with H_2 and stirred for 24 hours. Successful activation of H_2 would be the formation of

both P–H and B–H bonds. This would cause the appearance of B–H peaks around 2400 cm^{-1}, and P–H bonds in the 2200–2400 cm^{-1} range. Figure 3.5 shows no peaks in the 2200–2400 cm^{-1} range, indicating that the activation of H_2 was not successful. The large peak at 1000 cm^{-1} is indicative of bP oxidation. The set of peaks centered around 1500 cm^{-1} are the C–F stretches belonging to BCF as seen in previous spectra. The peak at 560 cm^{-1} is in the region for P–B bonds, suggesting the formation of the bP–BCF Lewis adduct that is not able to activate H_2. While we do not see H_2 activation, this reaction could be reversible. Future studies utilizing hydrogenation could investigate this more thoroughly.

3.3 CONCLUSIONS

Overall, the reactions confirm the successful formation of a classical Lewis adduct between bP and tris-pentafluorophenyl boron. However, this adduct was not able to access FLP reactivity through the activation of small molecules like H_2 and phenylacetylene as observed with some molecular phosphines. This could be due to the bP being a less sterically hindered phosphine. Perhaps the BCF bonding to the surface of a material as opposed to a molecular phosphine prevents the activation of small molecules.

3.4 EXPERIMENTAL

3.4.1 *Materials*

Unless stated otherwise, all work was performed under an inert atmosphere of N_2 using a Schlenk line or inside of an LC Technology Solutions, Inc. glove box containing <5 ppm H_2O and O_2. All

glassware was dried at 160℃ for a minimum of 12 h and cooled under vacuum prior to use. All solvents excluding benzonitrile were purchased from Fischer Scientific. Anhydrous solvents were dispensed from a JC Meyer solvent system and stored over 3 Å molecular sieves (Thermo-Fisher) for at least 12 h before use. Molecular sieves were previously activated under vacuum at 300℃ for 48 h. Benzonitrile (99%, Alfa Aesar) was degassed for at least 6 hours under vacuum and stored over activated 3Å molecular sieves in the glovebox for a minimum of 72 h prior to use.

Black phosphorus crystals were synthesized using the methods developed by Nilges.[6] Ultrasonication was performed in a 110 W bath sonicator at 40 kHz. Circulation cooling was used to maintain a bath temperature of 22-28℃. Filtrations were performed with EMD Millipore Omnipore hydrophobic membrane filters with a pore size of 0.2 μm. All reagents were stored in the glove box. Phenylacetylene (98+%, Thermo-Fisher) was purified by distillation and stored over 3 Å molecular sieves (Thermo-Fisher). Tris-pentafluorophenyl boron (97%, Stream) was stored in the glovebox.

3.4.2 *Instrumentation*

Attenuated total reflectance infrared (ATR-IR) spectra were recorded on a Bruker Alpha IR instrument equipped with a Platinum ATR accessory. Diffuse reflectance infrared Fourier transform spectroscopy (DRIFTS) was used in some analyses with the corresponding Bruker DRIFTS accessory and FTIR-grade potassium bromide (KBr, >99%; Alfa Aesar). ^{19}F-NMR was taken using 500MHz Avance NEO instrument.

3.4.3 *bP + BCF Control*

For the control reaction, 10 mg bP in benzonitrile was filtered using a 0.2 μm filter membrane and rinsed with toluene. The bP was redispersed in 20 mL of toluene by placing the filter paper

containing the bP into the vial with the toluene and sonicating for 1min. The filter paper was then rinsed and removed. In a separate vial, 1 eq of BCF was dissolved in 10 mL of toluene. Both the bP and BCF solutions were added to a Schlenk flask along with a stir bar. The flask was then transferred from the glove box to the Schlenk line where it was heated at 100 ˚C overnight.

After cooling to room temperature, the reaction flask was transferred back into the glove box for filtration. The mixture was filtered through 0.2 μm filter membrane and rinsed with 20 mL of toluene and 15 mL of pentane. The bP was resuspended in 10 mL of pentane by sonicating the filter paper in the pentane for 1min. The suspension was then centrifuged at 10,000 rpm in a microcentrifuge and dried under vacuum to remove any remaining pentane. The remaining solid was then analyzed by DRIFTS.

3.4.4 *FLP activation of PhCCH*

The solution exfoliated bP is stored in benzonitrile, so a solvent exchange is needed. The bP was made in a roughly 1 mg/mL solution. For a reaction requiring 20 mg of bP, 20 mL of solution were filtered using a 0.2 μm filter membrane and then rinsed with 20mL of toluene. The filter paper with the bP was placed in a vial with 10 mL of toluene and sonicated for a minute. After sonication the filter paper was rinsed with toluene and removed. To the bP solution, the PhCCH was added. In a separate vial, the BCF was weighed. The bP and PhCCH solution was added all at once to the vial containing the BCF and shaken until all the BCF was dissolved. The solution quickly turned dark red. An aliquot of the reaction mixture was passed through a filter. The filtrate was analyzed using NMR and ATR. The NMR samples were made with $CDCl_3$.

After the reaction was finished, the mixture was filtered using a 0.2 μm filter membrane. The filtered bP was rinsed with 10 mL of toluene followed by 10 mL of pentane. The bP was redispersed in pentane by placing the filter paper in a vial with 5 mL of pentane and sonicated for

1min. It was then dried by vacuum and analyzed using DRIFTS. The filtrate was saved in a scintillation vial to be analyzed by ATR and NMR.

3.4.5 *BCF + PhCCH Control Reaction*

In a 20 mL scintillation vial, 22 mg of PhCCH and 10 mL of toluene were added. To the vial, 90 mg of BCF was added all at once. The mixture was shaken until all the BCF was dissolved and the color had changed to dark reddish orange. The reaction mixture was immediately analyzed by ^{19}F-NMR and ATR.

3.4.6 *FLP activation of H_2*

15 mg of bP in benzonitrile was solvent exchanged with toluene by filtering the bP through a 0.2 µm filter membrane. After rinsing with 20 mL of toluene, the filter paper with the bP was added to a vial with 10mL of toluene and sonicated for 1min and the filter paper was removed. The bP in toluene was added to a round bottom Schlenk flask with a stir bar. A solution of 291.2 mg BCF in 5 mL of toluene was added to the round bottom flask. The flask was sealed and removed from the glove box and attached to the Schlenk line.

The Schlenk lines and flask headspace were purged and filled with H_2 five times. H_2 gas was then bubbled though the solution for 10 min. The flask was sealed, and the reaction was left stirring at room temperature for 24 h. An aliquot of the reaction mixture was filtered through a filter to be analyzed by NMR and ATR. The remaining mixture was filtered through a 0.2 µm filter membrane and rinsed with 20 mL of toluene and 20 mL of pentane. To redisperse the bP in pentane, the filter paper was added to a vial with 10 mL of pentane and sonicated for 1 min. It was then dried under vacuum until no solvent remained and analyzed by DRIFTS.

BIBLIOGRAPHY

(1) Shi, F.; Huang, K.; Feng, S. Recent Advances on Black Phosphorus Based Electrocatalysts for Water-Splitting. *ChemCatChem* **2020**, *12* (7), 1913–1921. https://doi.org/10.1002/cctc.201902288.

(2) Bridgman, P. W. TWO NEW MODIFICATIONS OF PHOSPHORUS. *J. Am. Chem. Soc.* **1914**, *36* (7), 1344–1363. https://doi.org/10.1021/ja02184a002.

(3) Liu, W.; Dong, A.; Wang, B.; Zhang, H. Current Advances in Black Phosphorus-Based Drug Delivery Systems for Cancer Therapy. *Adv. Sci.* **2021**, *8* (5), 2003033. https://doi.org/10.1002/advs.202003033.

(4) Hultgren, R.; Gingrich, N. S.; Warren, B. E. The Atomic Distribution in Red and Black Phosphorus and the Crystal Structure of Black Phosphorus. *J. Chem. Phys.* **1935**, *3* (6), 351–355. https://doi.org/10.1063/1.1749671.

(5) Keyes, R. W. The Electrical Properties of Black Phosphorus. *Phys. Rev.* **1953**, *92* (3), 580–584. https://doi.org/10.1103/PhysRev.92.580.

(6) Nilges, T.; Kersting, M.; Pfeifer, T. A Fast Low-Pressure Transport Route to Large Black Phosphorus Single Crystals. *J. Solid State Chem.* **2008**, *181* (8), 1707–1711. https://doi.org/10.1016/j.jssc.2008.03.008.

(7) Xia, F.; Wang, H.; Jia, Y. Rediscovering Black Phosphorus as an Anisotropic Layered Material for Optoelectronics and Electronics. *Nat. Commun.* **2014**, *5* (1), 4458. https://doi.org/10.1038/ncomms5458.

(8) Jin, Z.; Li, X.; Mullen, J. T.; Kim, K. W. Intrinsic Transport Properties of Electrons and Holes in Monolayer Transition-Metal Dichalcogenides. *Phys. Rev. B* **2014**, *90* (4), 045422. https://doi.org/10.1103/PhysRevB.90.045422.

(9) van Druenen, M.; Davitt, F.; Collins, T.; Glynn, C.; O'Dwyer, C.; Holmes, J. D.; Collins, G. Evaluating the Surface Chemistry of Black Phosphorus during Ambient Degradation. *Langmuir* **2019**, *35* (6), 2172–2178. https://doi.org/10.1021/acs.langmuir.8b04190.

(10) van Druenen, M.; Davitt, F.; Collins, T.; Glynn, C.; O'Dwyer, C.; Holmes, J. D.; Collins, G. Covalent Functionalization of Few-Layer Black Phosphorus Using Iodonium Salts and Comparison to Diazonium Modified Black Phosphorus. *Chem. Mater.* **2018**, *30* (14), 4667–4674. https://doi.org/10.1021/acs.chemmater.8b01306.

(11) Ryder, C. R.; Wood, J. D.; Wells, S. A.; Yang, Y.; Jariwala, D.; Marks, T. J.; Schatz, G. C.; Hersam, M. C. Covalent Functionalization and Passivation of Exfoliated Black Phosphorus via Aryl Diazonium Chemistry. *Nat. Chem.* **2016**, *8* (6), 597–602. https://doi.org/10.1038/nchem.2505.

(12) Yang, S.; Liu, Y.; Gao, P.; Zhang, T.; Zhu, X.; Zhang, M.; Chen, M.; Du, P.; Wang, G.-W.; Ji, H.; Yang, J. Azide Passivation of Black Phosphorus Nanosheets: Covalent Functionalization Affords Ambient Stability Enhancement. *Angew. Chem.* **2018**, ange.201813218. https://doi.org/10.1002/ange.201813218.

(13) Walz Mitra, K. L.; Chang, C. H.; Hanrahan, M. P.; Yang, J.; Tofan, D.; Holden, W. M.; Govind, N.; Seidler, G. T.; Rossini, A. J.; Velian, A. Surface Functionalization of Black Phosphorus with Nitrenes: Identification of P=N Bonds by Using Isotopic Labeling. *Angew. Chem. Int. Ed.* **2021**, *60* (16), 9127–9134. https://doi.org/10.1002/anie.202016033.

(14) Cho, S.-Y.; Koh, H.-J.; Yoo, H.-W.; Jung, H.-T. Tunable Chemical Sensing Performance of Black Phosphorus by Controlled Functionalization with Noble Metals. *Chem. Mater.* **2017**, *29* (17), 7197–7205. https://doi.org/10.1021/acs.chemmater.7b01353.

(15) Jeon, S.; Jia, J.; Ju, J. H.; Lee, S. Black Phosphorus Photodetector Integrated with Au Nanoparticles. *Appl. Phys. Lett.* **2019**, *115* (18), 183102. https://doi.org/10.1063/1.5119833.

(16) Qiao, H.; Liu, H.; Huang, Z.; Ma, Q.; Luo, S.; Li, J.; Liu, Y.; Zhong, J.; Qi, X. Black Phosphorus Nanosheets Modified with Au Nanoparticles as High Conductivity and High Activity Electrocatalyst for Oxygen Evolution Reaction. *Adv. Energy Mater.* **2020**, *10* (44), 2002424. https://doi.org/10.1002/aenm.202002424.

(17) Wang, X.; Bai, L.; Lu, J.; Zhang, X.; Liu, D.; Yang, H.; Wang, J.; Chu, P. K.; Ramakrishna, S.; Yu, X. Rapid Activation of Platinum with Black Phosphorus for Efficient Hydrogen Evolution. *Angew. Chem. Int. Ed.* **2019**, *58* (52), 19060–19066. https://doi.org/10.1002/anie.201911696.

(18) Vanni, M.; Serrano-Ruiz, M.; Telesio, F.; Heun, S.; Banchelli, M.; Matteini, P.; Mio, A. M.; Nicotra, G.; Spinella, C.; Caporali, S.; Giaccherini, A.; D'Acapito, F.; Caporali, M.; Peruzzini, M. Black Phosphorus/Palladium Nanohybrid: Unraveling the Nature of P–Pd Interaction and Application in Selective Hydrogenation. *Chem. Mater.* **2019**, *31* (14), 5075–5080. https://doi.org/10.1021/acs.chemmater.9b00851.

(19) Kuhl, O. Predicting the Net Donating Ability of Phosphines?Do We Need Sophisticated Theoretical Methods? *Coord. Chem. Rev.* **2005**, *249* (5–6), 693–704. https://doi.org/10.1016/j.ccr.2004.08.021.

(20) Zhao, Z.; Qin, F.; Kasiraju, S.; Xie, L.; Alam, M. K.; Chen, S.; Wang, D.; Ren, Z.; Wang, Z.; Grabow, L. C.; Bao, J. Vertically Aligned MoS_2 /Mo_2C Hybrid Nanosheets Grown on Carbon Paper for Efficient Electrocatalytic Hydrogen Evolution. *ACS Catal.* **2017**, *7* (10), 7312–7318. https://doi.org/10.1021/acscatal.7b02885.

(21) Castellanos-Gomez, A. Black Phosphorus: Narrow Gap, Wide Applications. *J. Phys. Chem. Lett.* **2015**, *6* (21), 4280–4291. https://doi.org/10.1021/acs.jpclett.5b01686.

(22) Li, W.; Liu, D.; Yang, N.; Wang, J.; Huang, M.; Liu, L.; Peng, X.; Wang, G.; Yu, X.-F.; Chu, P. K. Molybdenum Diselenide – Black Phosphorus Heterostructures for

Electrocatalytic Hydrogen Evolution. *Appl. Surf. Sci.* **2019**, *467–468*, 328–334. https://doi.org/10.1016/j.apsusc.2018.10.127.

(23) Huang, M.; Li, S.; Zhang, Z.; Xiong, X.; Li, X.; Wu, Y. Multifunctional High-Performance van Der Waals Heterostructures. *Nat. Nanotechnol.* **2017**, *12* (12), 1148–1154. https://doi.org/10.1038/nnano.2017.208.

(24) Deng, Y.; Luo, Z.; Conrad, N. J.; Liu, H.; Gong, Y.; Najmaei, S.; Ajayan, P. M.; Lou, J.; Xu, X.; Ye, P. D. Black Phosphorus–Monolayer MoS_2 van Der Waals Heterojunction p–n Diode. *ACS Nano* **2014**, *8* (8), 8292–8299. https://doi.org/10.1021/nn5027388.

(25) Mei, J.; Shang, J.; He, T.; Qi, D.; Kou, L.; Liao, T.; Du, A.; Sun, Z. 2D/2D Black Phosphorus/Nickel Hydroxide Heterostructures for Promoting Oxygen Evolution via Electronic Structure Modulation and Surface Reconstruction. *Adv. Energy Mater.* **2022**, *12* (25), 2201141. https://doi.org/10.1002/aenm.202201141.

(26) Lin, Y.; Pan, Y.; Zhang, J. In-Situ Grown of Ni 2 P Nanoparticles on 2D Black Phosphorus as a Novel Hybrid Catalyst for Hydrogen Evolution. *Int. J. Hydrog. Energy* **2017**, *42* (12), 7951–7956. https://doi.org/10.1016/j.ijhydene.2016.12.030.

(27) Wang, L.; Sofer, Z.; Pumera, M. Voltammetry of Layered Black Phosphorus: Electrochemistry of Multilayer Phosphorene. *ChemElectroChem* **2015**, *2* (3), 324–327. https://doi.org/10.1002/celc.201402363.

(28) Kephart, J. A.; Mitchell, B. S.; Kaminsky, W.; Velian, A. Multi-Active Site Dynamics on a Molecular Cr/Co/Se Cluster Catalyst. *J. Am. Chem. Soc.* **2022**, *144* (21), 9206–9211. https://doi.org/10.1021/jacs.2c00234.

(29) Masud, J.; Swesi, A. T.; Liyanage, W. P. R.; Nath, M. Cobalt Selenide Nanostructures: An Efficient Bifunctional Catalyst with High Current Density at Low Coverage. *ACS Appl. Mater. Interfaces* **2016**, *8* (27), 17292–17302. https://doi.org/10.1021/acsami.6b04862.

(30) Sun, J.; Li, J.; Li, Z.; Hu, X.; Bai, H.; Meng, X. Phase Transition in Cobalt Selenide with a Greatly Improved Electrocatalytic Activity in Hydrogen Evolution Reactions. *ACS Sustain. Chem. Eng.* **2022**, *10* (12), 4022–4030. https://doi.org/10.1021/acssuschemeng.2c00449.

(31) Ahmadian, F.; Salarvand, V.; Saghafi, M.; Noghani, M. T.; Yousefifar, A. Production and Characterization of High-Performance Cobalt–Nickel Selenide Catalyst with Excellent Activity in HER. *J. Mater. Res. Technol.* **2021**, *15*, 3942–3950. https://doi.org/10.1016/j.jmrt.2021.09.151.

(32) Zhang, X.; Wang, J.; Liu, D.; Zhang, Y.; Chu, P. K.; Zhou, Z.-Y.; Yu, X.-F. Insight into the Overpotentials of Electrocatalytic Hydrogen Evolution on Black Phosphorus Decorated with Metal Clusters. *Electrochimica Acta* **2020**, *358*, 136902. https://doi.org/10.1016/j.electacta.2020.136902.

(33) Li, Y.; Pei, W.; He, J.; Liu, K.; Qi, W.; Gao, X.; Zhou, S.; Xie, H.; Yin, K.; Gao, Y.; He, J.; Zhao, J.; Hu, J.; Chan, T.-S.; Li, Z.; Zhang, G.; Liu, M. Hybrids of PtRu Nanoclusters and

Black Phosphorus Nanosheets for Highly Efficient Alkaline Hydrogen Evolution Reaction. *ACS Catal.* **2019**, *9* (12), 10870–10875. https://doi.org/10.1021/acscatal.9b03506.

(34) Elgrishi, N.; Rountree, K. J.; McCarthy, B. D.; Rountree, E. S.; Eisenhart, T. T.; Dempsey, J. L. A Practical Beginner's Guide to Cyclic Voltammetry. *J. Chem. Educ.* **2018**, *95* (2), 197–206. https://doi.org/10.1021/acs.jchemed.7b00361.

(35) Fourmond, V.; Jacques, P.-A.; Fontecave, M.; Artero, V. H_2 Evolution and Molecular Electrocatalysts: Determination of Overpotentials and Effect of Homoconjugation. *Inorg. Chem.* **2010**, *49* (22), 10338–10347. https://doi.org/10.1021/ic101187v.

(36) Treimer, S. E.; Evans, D. H. Electrochemical Reduction of Acids in Dimethyl Sulfoxide. CE Mechanisms and Beyond. *J. Electroanal. Chem.* **1998**, *449* (1–2), 39–48. https://doi.org/10.1016/S0022-0728(97)00478-6.

(37) Jensen, W. B. The Lewis Acid-Base Definitions: A Status Report. *Chem. Rev.* **1978**, *78* (1), 1–22. https://doi.org/10.1021/cr60311a002.

(38) Tofan, D.; Sakazaki, Y.; Walz Mitra, K. L.; Peng, R.; Lee, S.; Li, M.; Velian, A. Surface Modification of Black Phosphorus with Group 13 Lewis Acids for Ambient Protection and Electronic Tuning. *Angew. Chem. Int. Ed.* **2021**, *60* (15), 8329–8336. https://doi.org/10.1002/anie.202100308.

(39) McCahill, J. S. J.; Welch, G. C.; Stephan, D. W. Reactivity of "Frustrated Lewis Pairs": Three-Component Reactions of Phosphines, a Borane, and Olefins. *Angew. Chem. Int. Ed.* **2007**, *46* (26), 4968–4971. https://doi.org/10.1002/anie.200701215.

(40) Stephan, D. W. Frustrated Lewis Pairs. *J. Am. Chem. Soc.* **2015**, *137* (32), 10018–10032. https://doi.org/10.1021/jacs.5b06794.

(41) Dureen, M. A.; Stephan, D. W. Terminal Alkyne Activation by Frustrated and Classical Lewis Acid/Phosphine Pairs. *J. Am. Chem. Soc.* **2009**, *131* (24), 8396–8397. https://doi.org/10.1021/ja903650w.

(42) Stephan, D. W. Diverse Uses of the Reaction of Frustrated Lewis Pair (FLP) with Hydrogen. *J. Am. Chem. Soc.* **2021**, *143* (48), 20002–20014. https://doi.org/10.1021/jacs.1c10845.

(43) Dureen, M. A.; Brown, C. C.; Stephan, D. W. Addition of Enamines or Pyrroles and $B(C_6F_5)_3$ "Frustrated Lewis Pairs" to Alkynes. *Organometallics* **2010**, *29* (23), 6422–6432. https://doi.org/10.1021/om1008346.

(44) Liu, S.; Dong, M.; Wu, Y.; Luan, S.; Xin, Y.; Du, J.; Li, S.; Liu, H.; Han, B. Solid Surface Frustrated Lewis Pair Constructed on Layered AlOOH for Hydrogenation Reaction. *Nat. Commun.* **2022**, *13* (1), 2320. https://doi.org/10.1038/s41467-022-29970-6.

(45) Ghuman, K. K.; Wood, T. E.; Hoch, L. B.; Mims, C. A.; Ozin, G. A.; Singh, C. V. Illuminating CO_2 Reduction on Frustrated Lewis Pair Surfaces: Investigating the Role of

Surface Hydroxides and Oxygen Vacancies on Nanocrystalline In $_2$ O $_{3-x}$ (OH) $_y$. *Phys. Chem. Chem. Phys.* **2015**, *17* (22), 14623–14635. https://doi.org/10.1039/C5CP02613J.

(46) Clavier, H.; Nolan, S. P. Percent Buried Volume for Phosphine and N-Heterocyclic Carbene Ligands: Steric Properties in Organometallic Chemistry. *Chem. Commun.* **2010**, *46* (6), 841. https://doi.org/10.1039/b922984a.

(47) Anaya de Parrodi, C.; Walsh, P. J. All Kinds of Reactivity: Recent Breakthroughs in Metal-Catalyzed Alkyne Chemistry. *Angew. Chem. Int. Ed.* **2009**, *48* (26), 4679–4682. https://doi.org/10.1002/anie.200900900.

(48) Boyall, D.; Frantz, D. E.; Carreira, E. M. Efficient Enantioselective Additions of Terminal Alkynes and Aldehydes under Operationally Convenient Conditions. *Org. Lett.* **2002**, *4* (15), 2605–2606. https://doi.org/10.1021/ol026282k.

(49) *Ionic Liquids: Industrial Applications for Green Chemistry*; Rogers, R. D., Seddon, K. R., Eds.; ACS Symposium Series; American Chemical Society: Washington, DC, 2002; Vol. 818. https://doi.org/10.1021/bk-2002-0818.

(50) Ohmiya, H.; Yorimitsu, H.; Oshima, K. Cobalt-Catalyzedsyn Hydrophosphination of Alkynes. *Angew. Chem.* **2005**, *117* (16), 2420–2422. https://doi.org/10.1002/ange.200500255.

(51) Jiang, C.; Blacque, O.; Berke, H. Activation of Terminal Alkynes by Frustrated Lewis Pairs. *Organometallics* **2010**, *29* (1), 125–133. https://doi.org/10.1021/om9008636.

(52) Marques, L. R.; Ando, R. A. Infrared Spectroscopy Evidence of Weak Interactions in Frustrated Lewis Pairs Formed by Tris(Pentafluorophenyl)Borane. *ChemPhysChem* **2022**. https://doi.org/10.1002/cphc.202200715.

(53) Welch, G. C.; Juan, R. R. S.; Masuda, J. D.; Stephan, D. W. Reversible, Metal-Free Hydrogen Activation. *Science* **2006**, *314* (5802), 1124–1126. https://doi.org/10.1126/science.1134230.

(54) Thomas, L. C. *Interpretation of the Infrared Spectra of Organophosphorus Compounds*; Heyden & Son Ltd., 1974.